Interferometric height estimation of the seafloor via synthetic aperture sonar in the presence of motion errors

W.W.Bonifant, Jr., M.A.Richards and J.H.McClellan

Abstract: An end-to-end simulated processing chain related to an existing synthetic aperture sonar (SAS) system is developed and described, including motion compensation, efficient image formation and autofocus procedures. The processing is extended to include interferometric height estimation capability. It is the goal of the paper to study the application of interferometry to SAS systems in the presence of motion errors. The system is analysed with respect to motion errors and the subsequent damaging effects to both imaging and height estimation. Results using both measured and simulated data are presented. The problem is addressed with respect to both one-pass and two-pass imaging geometries, and it is hypothesised that for slowly varying target height, one-pass SAS interferometry may be a more robust imaging tool than conventional SAS alone. The simulated results suggest that height information is recoverable even in some situations in which the conventional SAS reflectivity image is completely ruined by phase error induced blur. High-resolution SAS imaging coupled with interferometric height estimation for seafloor imaging has military applicability in mine detection or classification and in topographic mapping in preparation for an amphibious assault. Civilian uses would include surveying of objects such as oil pipelines and seabed mapping.

1 Introduction

Sidelooking stripmap synthetic aperture radar (SAR) and sonar (SAS) processing are imaging techniques that map the complex reflectivity of a target area on land or on the sea bottom. The platform, whether it is a satellite or aircraft (for SAR), or a towfish (for SAS), traverses a theoretically straight-line track, as shown in Fig. 1, while transmitting successive, equally spaced signals in a beam aimed perpendicular to the track. These signals reflect back from the target area to the platform, where they are collected to form a data matrix. The magnitude of an example SAS data matrix for a singular point target at 200 metres is shown in Fig. 2.

These target responses are range-variant, in that the response curvature is more pronounced at closer range. The synthetic aperture imaging problem is to invert the

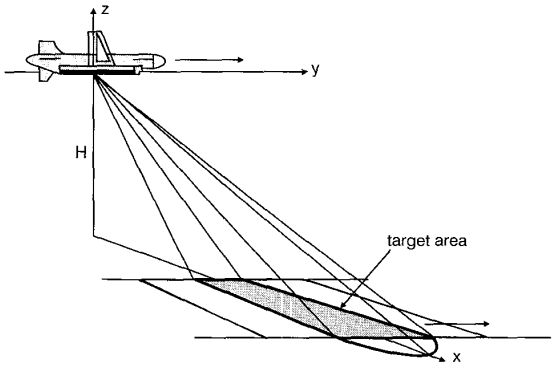

Fig. 1 *Synthetic aperture imaging geometry*

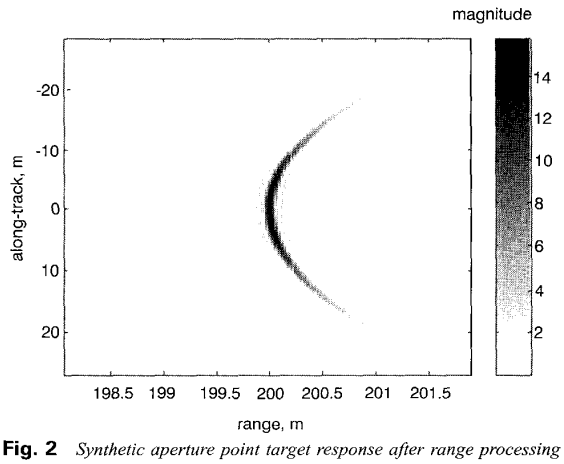

Fig. 2 *Synthetic aperture point target response after range processing*

IEE Proceedings online no. 20000618

DOI: 10.1049/ip-rsn:20000618

Paper first received 17th September 1999 and in revised form 11th May 2000

W.W. Bonifant was with the Georgia Tech Research Institute and is now on active duty with the US Navy

M.A. Richards is with the Radar Systems Division, Sensors and Electromagnetic Applications Laboratory (SEAL), Georgia Tech Research Institute (GTRI), 7220 Richardson Road, Building 5, Smyrna, GA 30080, USA

J.H. McClellan is with the Electrical and Computer Engineering Department, Center for Signal and Image Processing, School of Electrical and Computer Engineering, Georgia Institute of Technology, Atlanta, GA 30332-0250, USA

superposition of all target responses into correctly located impulses. Utilising synthetic aperture processing, it is possible to obtain an image that has azimuthal resolution δ^y_{SA} independent of range and signal frequency, and that is only dependent upon the real aperture size D ([1], ch. 10)

$$\delta^y_{SA} = D/2 \tag{1}$$

This is a significant advantage over conventional, real aperture processing.

Radar systems have been utilising the technique since the 1950s and many systems currently exist for a variety of applications. Though conceptually the same as synthetic aperture radar (SAR), SAS has been slower to mature for a number of reasons. Initially, it was thought that instability of the ocean medium would limit the formation of a synthetic aperture, but tests during the 1970s and 1980s [2–4] showed that phase coherency is typically adequate over the aperture integration period. Due to the relatively slow propagation speed of sound through water, unambiguous range combined with aperture sampling requirements limit SAS platform speed, exacerbating motion errors and limiting the system mapping rate [5]. Several methods have been suggested, e.g. multiaperture system geometries [5], wideband signal transmission [6], to allow increased platform velocity while reducing aperture undersampling or its effects. Finally, motion errors are more pronounced in SAS than in SAR due to the turbulent media and slower platform speed. Many methods have been proposed to combat this problem and the specific procedure we use is outlined in this paper. Sonar systems that utilise synthetic aperture processing are primarily experimental, and few open-ocean systems exist worldwide. It is expected that future applications will include mine detection and classification, and surveying for such things as oil pipelines or shipwrecks. An excellent review of SAS history and development can be found in [7].

Interferometry [8] is a technique commonly used by SAR systems to estimate terrain height by utilising the phase difference information between two synthetic aperture images formed from different aspect angles. The technique was proposed for SAS as early as 1983 [9], and has recently seen increased interest, including experimental demonstrations for SAS [10]. Real-world implementation of the technique would extend the application and utility of SAS imaging. For example, prior to an amphibious landing, it is highly desirable to have knowledge of the undersea topography near the beach. It is the goal of this paper to study the application of interferometry to SAS systems in the presence of motion errors. Based on an end-to-end simulation of a state-of-the-art SAS system, the DARPA (Defense Advanced Research Projects Agency, an agency of the United States Dept. of Defense) SAS [10], we investigate the application of interferometric height estimation for ocean bottom mapping. Specifically, we analyse the effects of motion and phase errors and some methods to remove those errors. More details about this study can be found in [11].

2 Range ambiguity and along-track sampling rate

A fundamental SAS imaging constraint derives from the relationship between unambiguous range and along-track sampling requirements. This problem was described early in the articles by Cutrona, 1975 [5], Williams, 1976 [12] and Lee, 1979 [13], and recently in the article by Griffiths, *et al.*, 1997 [9]. There have been a number of methods proposed to minimise this problem, a summary of which is given in [14]. We review the problem here, and describe the steps taken by the DARPA SAS to overcome it.

To avoid range ambiguities, it is necessary to transmit pulses at a rate that relates to the swath length via

$$PRF \leq \frac{c}{2X_s} \tag{2}$$

where X_s is the swath length in range, PRF is the pulse repetition frequency, the periodic rate at which signals are transmitted and c is the speed of sound in water. Letting v_p be the platform along-track velocity and Δ_u be the along-track sample spacing (in metres), the PRF is given by

$$PRF = v_p/\Delta_u \tag{3}$$

It is necessary to adequately sample the aperture in along-track to avoid deleterious undersampling effects such as grating lobes. The SAR community has long regarded an along-track sample spacing of $\Delta_u = D/2$ to be sufficient, where D is the physical aperture length. This sample spacing causes the nulls in the real aperture beam pattern to occur at grating lobe locations, thus suppressing them [15]. However, it was shown in [16], App. A and in [17], p.293 that $D/2$ spacing only partially suppresses the grating lobes and that $D/4$ spacing is necessary for complete elimination. By inserting this requirement into eqn. 3 and rearranging eqn. 2, we arrive at a maximum platform velocity for a given swath extent

$$v_{P_{\max}} = \frac{cD}{8X_s} \tag{4}$$

Since along-track resolution is directly related to real aperture size, there is an interrelationship between resolution, maximum unambiguous range and platform velocity based on eqn. 4, shown in Fig. 3, where it is assumed that X_s goes from zero to the maximum range. The contours represent along-track resolution. The DARPA SAS can operate with an along-track resolution of approximately 5 or 10 cm and is intended to unambiguously image ranges of up to 1 km. At large ranges, a single transmitter/single receiver geometry would require an extremely low platform velocity for this system. This would exacerbate motion errors and limit the system mapping rate.

To combat the problem, the DARPA SAS utilises a relatively wide bandwidth signal (10 kHz on a 50 kHz carrier). This 'smears out' the grating lobe energy, which is signal frequency dependent [16]. Additionally, the system employs a single transmitter with 16 along-track

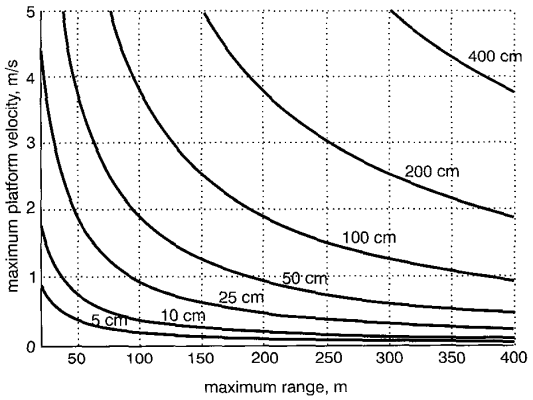

Fig. 3 *SAS parameter relationships*

Along-track resolution is shown as a function of maximum unambiguous range and maximum platform velocity for a sample spacing $= D/4$

receivers to fill in the along-track samples that would be missed by a single-receiver platform travelling at the same velocity. This is sometimes called the *vernier* technique, and has been suggested by Kock [18] and Gilmour [19], and also in [13]. The idea itself is relatively simple. For a given transmitter and receiver which are separated by a small distance, we can assume that an equivalent pair exists midway between them. This is called a *displaced phase centre* [20] and is shown in the lower right portion of Fig. 4. The upper left portion of the Figure shows how the concept is used to fill in the data matrix.

This assumption is an approximation that can be accounted for by an extra phase correction in the data matrix [11]. Since each displaced phase centre is located halfway between the corresponding transmitter and receiver, the signal returns from a system with N receivers of width D can be used to employ a sample spacing of $D/2$. The velocity of the system is constrained by

$$v_p = \frac{ND}{2} \cdot PRF \tag{5}$$

and the ambiguity relationship given in eqn. 4 improves to

$$v_{p_{\max}} = \frac{cD}{4X_s} \cdot N \tag{6}$$

Note that by employing this method, we give up $D/4$ sample spacing and settle for $D/2$. In return, we double the tow speed possible for a given range swath size, an important factor in minimising some motion errors. The DARPA SAS data available for this research employed $D/2$ spacing. The grating lobes were limited to a tolerable level of -40 dB by the wideband signal used. Consequently, we use $D/2$ sampling for the remaining simulations and measured data processing.

3 SAS image processing

The processing chain used in this study for synthetic aperture imaging is shown in Fig. 5. We describe each of the processing steps below, in preparation for our discussion on interferometry.

3.1 Generation and compression of data

The raw data used for analysis was obtained by two methods. The first method was to create a synthetic raw data set using the raw data expression [16]

$$ee(t,u) \approx \int_x \int_y ff(x,y) \cdot (a(t,x,y-u)^*{}_t \ldots$$

$$\ldots {}^*{}_t p_m\left(t - \frac{2}{c}\sqrt{x^2 + (y-u)^2}\right)\right) dxdy \tag{7}$$

where t and u are the temporal and along-track variables, respectively, $ff(x, y)$ is the target reflectivity distribution, $a(t, x, y)$ is the transmit-and-receive aperture radiation pattern function and $p_m(t)$ is the transmitted signal function, including both the modulation and the carrier terms. The second method was to use measured data collected by the DARPA SAS.

The first processing step was pulse compression via range-matched filtering, so that each target in the data displayed the range-variant hyperbolic response shown in Fig. 2. Two assumptions we have made about the data matrix must be corrected at this point, if efficient imaging algorithms are to be utilised. First, we have assumed that the displaced phase centres fall directly between the transmitter and receivers, as discussed in the previous Section, when in actuality, the round-trip propagation distance is slightly greater for the actual transmitter and receiver than for the assumed displaced phase centre. Secondly, we have assumed that the platform is stationary during each signal pulse propagation. Both of these assumptions are not true, introducing additional, undesired phase terms into the data. Uncorrected, the image will contain spurious sidelobes. In [11], a phase multiplication was derived to correct for these errors, based on an exact correction for a target located at the scene centre.

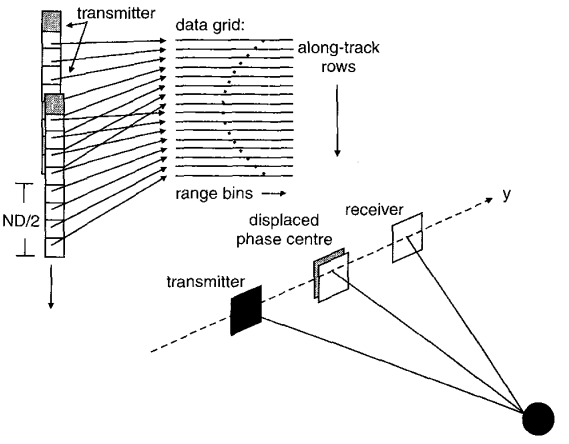

Fig. 4 *Displaced phase centre concept*

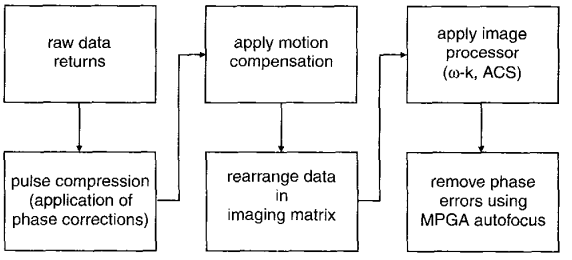

Fig. 5 *SAS processing flow*

3.2 Motion compensation

The towfish can be affected by six degrees of motion, as shown in Fig. 6. The degrees of motion that most severely affect the formation of the reflectivity image are yaw and sway, since they affect the range dimension. For this reason, we assumed that all other degrees of errant towfish motion were well behaved when applying motion compensation techniques. This was typically the case for the measured data sets studied. Correction of these errors required a two-part motion compensation routine.

Sway errors were estimated via the displaced phase centre algorithm [21], a correlation-based technique based on the following principle. Assuming that a phase centre exists exactly halfway between the transmitter and each receiver, the platform velocity can be selected so that some phase centres overlap from ping to ping, providing redundant information. This concept is shown in Fig. 7.

Yaw errors were estimated using a method similar to that suggested in [22]. For each group of adjacent pings, two 2-D matrices of angle and time were formed using standard beamforming operations. These matrices were cross-corre-

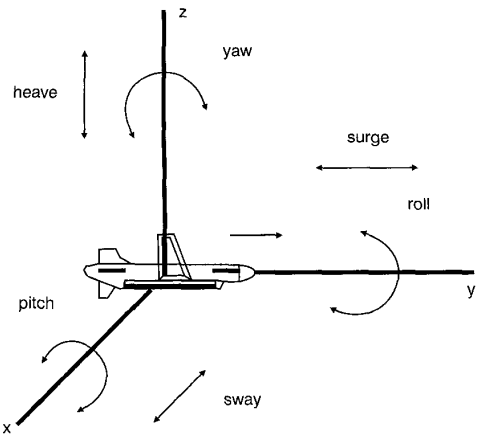

Fig. 6 *Degrees of errant towfish motion*

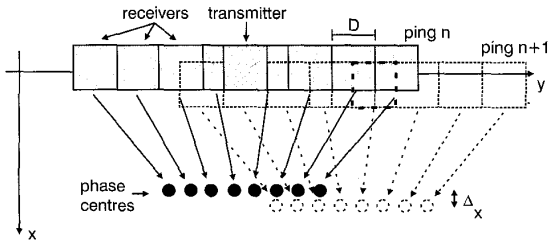

Fig. 7 *Overlapping of phase centres for sway estimation*

lated to yield the relative angular displacement of the platform for each adjacent set of pings.

3.3 Image formation

Most experimental SAS imaging systems found in the literature use explicit matched filtering operations to focus the data. That is, each target in the scene is focused based on the exact 2-D matched filter for that location. This approach is very computationally expensive. Other SAR imaging algorithms that are more efficient for single sensor data can successfully be applied to SAS [16] and may be necessary for real-time implementation of SAS by less expensive systems. Two of these, the seismic migration (or ω–k) [23] and the accelerated chirp scaling [24] algorithms, were alternately used as image formation steps in our study. To apply these algorithms, it is necessary that the data be sampled on a uniformly spaced 2-D grid. Thus, before image focusing, the data was resampled and interpolated, if necessary, to satisfy this requirement. However, interpolation with reasonable quality is itself a computationally intensive process, and we have made no systematic comparison of the computational requirements of these various imaging algorithms.

3.4 Application of PGA autofocus

Following image formation, it was necessary to remove any residual phase errors. Estimation and correction of these errors utilising information within the image data is called autofocus. In the SAR community, the phase gradient autofocus (PGA) [25] algorithm has demonstrated robust success over a wide variety of images, where it is assumed that each target in the scene is affected by an identical phase error function. The algorithm begins by circularly shifting the brightest scatterer on each range line to the scene centre. Then, the data set is windowed and Fourier transformed in along-track, at which point the error function is estimated by calculating and integrating the phase differences between pixels in the along-track dimension. To ensure robustness, this operation is coherently averaged over range. The image is corrected based on the estimated error function.

It would be desirable to use PGA for correction of SAS data sets, but unfortunately, it was developed using an error model for spotlight SAR, i.e. for systems that slew the antenna so that the beam is constantly pointed at the same location. Ignoring noise, the PGA error model for a single point target at (x_0, y_0) is given by [26]

$$g_\delta(x, y) \approx a(x_0, y_0)^*{}_y h(y) \tag{8}$$

where the complex reflectivity of each point target $a(x_0, y_0)$ is convolved with an identical image blurring function $h(y) = IFFT_y\{\exp(j\Phi(k_y))\}$. $\Phi(k_y)$ is an along-track frequency blurring function, and x and y are the range and along-track variables, respectively. The along-track Fourier domain is represented by the wavenumber k_y.

All existing SAS systems utilise stripmap imaging, i.e. the beam is held perpendicular to the track during the integration period. We would like to derive an error model for these systems based on an along-track lateral error function $\Delta(u)$. Inserting this error term into eqn. 7 yields, for a point target located at (x_0, y_0)

$$ee_{m_\delta}(t, u) \approx \alpha \int d\omega P_m(\omega) \cdot \exp\left(-j2\frac{\omega}{c}\sqrt{(x_0 - \Delta(u))^2 + (y_0 - u)^2}\right) \cdot \exp(j\omega t) \tag{9}$$

where $P_m(\omega)$ is the range frequency domain signal expression and α is the reflectivity of the point target. We can further approximate the effect of the error function by a phase multiplication using an exponential containing the error term to give

$$ee_{m_\delta}(t, u) \approx \alpha \int d\omega P_m(\omega) \cdot \exp\left(-j2\frac{\omega}{c}\sqrt{x_0^2 + (y_0 - u)^2}\right) \cdot \exp\left(j2\frac{\omega}{c}\Delta(u)\right)\exp(j\omega t) \tag{10}$$

We next assume $\Delta(u)$ to be small, and sufficiently slowly varying such that $\Delta(u)$ varies with u more slowly than does range. The 2-D frequency expression for eqn. 10 can then be found by utilising the principle of stationary phase (PSP) [27] and is given by

$$EE_{m_\delta}(\omega, k_y) \approx \alpha P_m(\omega)\exp(-jk_x x_0 - jk_y y_0) \cdot \exp\left(j2\frac{\omega}{c}\Delta\left(y_0 - \frac{k_y}{k_x}x_0\right)\right) \tag{11}$$

where k_y is the along-track frequency variable and k_x is a wavenumber described by

$$k_x = \sqrt{\left(2\frac{\omega}{c}\right)^2 - k_y^2} \tag{12}$$

A complex constant that arises in the application of the PSP has been absorbed into the target amplitude constant α.

The focused image can be described by applying the following 2-D frequency-dependent matched filter

$$HH_0 = P_m^*(\omega)\exp(-jk_y y - jk_x x) \tag{13}$$

to the data. Applying this operation to eqn. 11. and then taking the 2-D inverse Fourier transform yields

$$gg_\delta(x,y) \approx \alpha \int\int dk_x dk_y \exp(jk_y(y-y_0) + \ldots$$
$$+ jk_y(x-x_0))\exp\left(j2\frac{\omega}{c}\Delta\left(y_0 - \frac{k_y x_0}{k_x}\right)\right) \tag{14}$$

where we have assumed that $|P_m(\omega)|^2 \equiv 1$ over the signal bandwidth.

We can think of eqn. 14 as the ideal image response multiplied in the 2-D frequency domain by some phase error function that varies with target location. At first glance, it does not appear that this expression is similar to eqn. 8. However, because the signal is transmitted on a modulated carrier, eqn. 12 is larger in magnitude than k_y (i.e. $|k_x/k_y| \gg 1$) and the phase error function is essentially independent of target range location. For small lateral motion errors, the phase error function only causes the image to blur in the along-track dimension. Therefore, for situations in which the function $\Delta(u)$ is small and slowly varying in along-track, we can apply the spotlight PGA algorithm in the following manner. First, the image is divided in along-track into many overlapping strips. The PGA algorithm is applied to each strip, the data is corrected, and the appropriate sections are pieced together to form the new image. We call this 'mosaic PGA' (MPGA).

Another stripmap PGA autofocus procedure was proposed in [28] by the developers of the PGA algorithm. This procedure assumes that convolution of the image data with an appropriate along-track chirp will restore the original pulse-compressed data matrix, effectively making a narrowband assumption that the range migration is much less than a resolution cell. For SAS parameters, this assumption breaks down and this operation would restore the range-migration corrected data matrix [29]. The targets are not circularly shifted, and any target selected is used to estimate the phase error function for its local along-track location. The spotlight version of PGA utilises redundancy over range [25] to estimate the phase error function through the coherent averaging operation. The proposed algorithm of [28], however, offers no metric for the selection of bright scatterers, and even if the brightest scatterer on each range line is chosen, offers no guarantee that conditions will exist for sufficient averaging over range bins. That is, since the data is not circularly shifted, any bright targets would be likely to be scattered throughout the scene. Our method, by dividing the data into strips and applying the spotlight version of PGA to each strip, ensures that the robust redundancy over range of the spotlight PGA algorithm is preserved.

In practice, our motion compensation suite reduced the errors to the point where autofocus could be applied. Fig. 8 shows focused measured-data imagery for a collection of point-like targets at a range of over 200 m. For Fig. 8*a*, no motion compensation or autofocus was used. For Fig. 8*b*, motion compensation was applied, but not autofocus. Finally, for Fig. 8*c*, PGA autofocus was used in the manner described above. The improvement with the addition of each processing step is evident. The image in Fig. 8*d* was formed via conventional sonar beamforming of the data from the 16-hydrophone array to accentuate the tremendous resolution advantage of SAS processing.

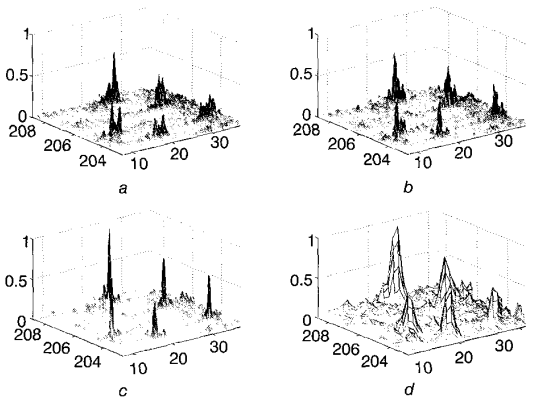

Fig. 8 *Focused imagery from measured data*

4 Interferometric height estimation

The interferometric geometry is shown in Fig. 9 and the problem is outlined below. The scene is imaged by two apertures displaced from one another and therefore at slightly different depression angles with respect to the scene, and the system parameters B, ζ and H are assumed to be known. The slant range from the lower aperture r_1 to each pixel is found from the corresponding SAS image. The second image is then precisely coregistered with the first image, or resampled to exactly the same imaging plane, so that the exact slant range r_2 can be calculated from the pixel-to-pixel phase difference between images based on the known signal wavelength. Many image registration techniques can be found in the literature, and we adopt a method described in [30]. These phase differences are measured modulo 2π, so a 2-D phase unwrapping algorithm such as the one described in [31] is needed to calculate the absolute phase differences. Once both slant ranges are known, it is straightforward to calculate the corresponding target height based on the given geometry [9].

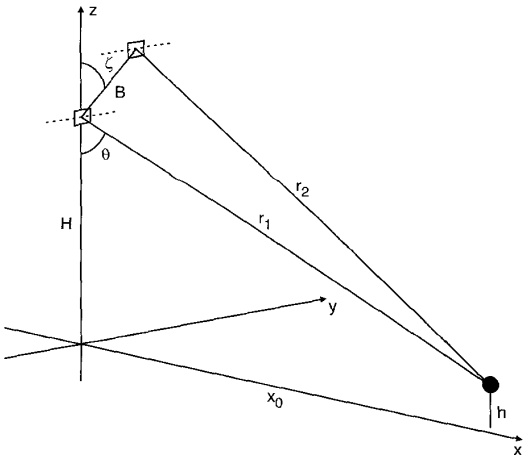

Fig. 9 *Interferometric imaging geometry*

5 Effect of motion errors on interferometry

Based on processing of simulated data, we studied the effect of motion errors on interferometric SAS using two different common imaging geometries. In a one-pass system, both apertures are contained on the same platform and a single transmitter is used. In a two-pass system, the same aperture traverses separate tracks at different times, which would allow for a much larger aperture displacement. It has been suggested [9] that two-pass interferometry will be very difficult to implement with SAS systems. We analyse the problem here to confirm this hypothesis.

All previous interferometric error sensitivity studies have been performed with respect to specific system parameters (e.g. [9, 32, 33]). That is, the partial derivative of the height estimate is taken with respect to each parameter, based on the geometry of Fig. 9. This has been a basis for studies on interferometric system design [33]. However, this does not adequately describe the effect of motion errors, since errant platform motion will affect many parameters simultaneously. Some simulation results with respect to motion errors were given in [9], but no analysis. We analysed the problem in two ways and the methodology and results are discussed below.

5.1 Geometric analysis

First, we analysed the problem based solely on the imaging geometry of Fig. 9. Given that the height estimate can be described by [33]

$$h = H - r_1\left[\cos\xi\sqrt{1-\sin^2(\theta-\xi)} - \sin\xi\sin(\theta-\xi)\right] \tag{15}$$

where $\xi = \pi/2 - \zeta$ we derived an error function

$$\varepsilon_h = h - \hat{h} = H - \hat{H} + \frac{1}{2B}\left[\begin{array}{l}(\hat{r}_2^2 - \hat{r}_1^2 - (r_2^2 - r_1^2))\cos\zeta - \cdots \\ \quad \cdots - \left(\sqrt{(2r_1B)^2 - (r_2^2 - r_1^2 - B^2)^2} - \cdots\right. \\ \quad \left. \cdots - \sqrt{(2\hat{r}_1B)^2 - (\hat{r}_2^2 - \hat{r}_1^2 - B^2)^2}\right)\sin\zeta\end{array}\right] \tag{16}$$

to describe the height estimation error based on erroneous measurements due to motion. An overhat represents a measured rather than an actual parameter. Notice that if the tilt angle ζ is zero (vertical aperture displacement), this equation simplifies to

$$\varepsilon_h = [\hat{r}_2^2 - \hat{r}_1^2 - (r_2^2 - r_1^2)]/2B \tag{17}$$

By holding appropriate parameters constant and allowing others to vary, we were able to derive the following expressions for height error based on a motion error Δ relative to both apertures in a two-pass geometry, in all three directions. To simplify the expressions for clarity, we assumed vertical aperture displacement. That is, the measured parameters in eqn. 17 were corrupted by some error Δ and the following expressions were derived. To demonstrate the effects of relative error between apertures, we assumed that only the lower aperture was affected.

Errors in range (two-pass):

$$\begin{aligned}\varepsilon_h^x &= \frac{1}{2B}\left(\left(\sqrt{(H-h)^2 + x_0^2}\right)^2 - \left(\sqrt{(H-h)^2 + (x_0 - \Delta_x)^2}\right)^2\right) \\ &= \frac{1}{2B}(2x_0\Delta_x - \Delta_x^2)\end{aligned} \tag{18}$$

Errors in altitude (two-pass):

$$\begin{aligned}\varepsilon_h^z &= H - \hat{H} + \frac{1}{2B}\left(\left(\sqrt{(H-h)^2 + x_0^2}\right)^2 - \left(\sqrt{(H-h+\Delta_z)^2 + x_0^2}\right)^2\right) \\ &= H - \hat{H} + \frac{1}{2B}(\hat{r}_1^2 - r_1^2) \\ &= \frac{1}{2B}((2H - 2h)\Delta_z + \Delta_z^2) - \Delta_z\end{aligned} \tag{19}$$

Errors in along-track (two-pass):

$$\begin{aligned}\varepsilon_h^y &= \frac{1}{2B}\left(r_1^2 - \left(\sqrt{r_1^2 + \Delta_y^2}\right)^2\right) \\ &= -\Delta_y^2/2B\end{aligned} \tag{20}$$

As expected, the sensitivity to motion errors is inversely proportional to system baseline, based on this geometric analysis. This suggests that a two-pass system would perform better than a one-pass system because it has the flexibility to employ large aperture separation. However, this does not take into account the increased image-to-image decorrelation [33] and decreased interferometric fringe spacing [11] associated with large baseline geometries. Also, since eqn. 18 is target-range dependent, range errors most severely affect height estimation in two-pass imaging.

A similar analysis was performed for one-pass interferometry, where it was taken into account that both apertures are located on the same platform. For the cases of sway, yaw, and surge, the error terms inserted into eqn. 16 cancel out because they are identical for both apertures, leaving a resultant error of zero. For example, for lateral errors

$$\begin{aligned}\hat{r}_1 &= \sqrt{(H-h)^2 + (x_0 - \Delta_x)^2}; \\ \hat{r}_2 &= \sqrt{(H+B-h)^2 + (x_0 - \Delta_x)^2}\end{aligned} \tag{21}$$

$$\varepsilon_h^x = \left(\frac{1}{2B}\right)(\hat{r}_2^2 - \hat{r}_1^2 - (r_2^2 - r_1^2)) = 0 \tag{22}$$

For the cases of pitch and heave, there will be a relative height estimate error based upon the H terms in eqn. 16. For heave errors, the rest of the error terms cancel out for the same reasons as for sway, yaw and surge. For pitch, the error term does not cancel out, but the additional effect is almost negligible since the difference in motion affecting both apertures is very slight.

These results are surprising, and suggest that these degrees of motion have a relatively small effect on one-pass interferometry based on the system geometry. Note that at the same time, the individual reflectivity image may be severely corrupted due to the errant platform motion.

Roll errors, assuming that the axis of rotation is between the apertures, have a significant impact on one-pass interferometry, since the apertures are affected by the same motion but in opposite directions, as shown in Fig. 10. The corrupted slant ranges and corresponding height estimate error become

$$\hat{r}_1 = \sqrt{\left(H - h - \left(\frac{B}{2} - \frac{B}{2}\cos\Delta_\zeta\right)\right)^2 + \left(x_0 + \frac{B}{2}\sin\Delta_\zeta\right)^2} \tag{23}$$

$$\hat{r}_2 = \sqrt{\left(H - h + \left(\frac{B}{2} - \frac{B}{2}\cos\Delta_\zeta\right)\right)^2 + \left(x_0 - \frac{B}{2}\sin\Delta_\zeta\right)^2} \tag{24}$$

Roll Errors (one-pass):

$$\begin{aligned}\varepsilon_h^{roll} = \frac{1}{2B}[&(H - h - B/2)^2 + x_0^2 - (H - h + B/2)^2 \\ &- x_0^2 - \ldots - (H - h - B/2 + B/2\cos\Delta_\zeta)^2 \\ &- (x_0 + B/2\sin\Delta_\zeta)^2 + \ldots \\ &+ (H - h + B/2 - B/2\cos\Delta_\zeta)^2 \\ &+ (x_0 - B/2\sin\Delta_\zeta)^2] \\ = h\cos\Delta_\zeta &- H\cos\Delta_\zeta - x_0\sin\Delta_\zeta\end{aligned} \tag{25}$$

Based on this geometric analysis, roll errors are the only motion that severely affect the height estimate. This suggests that, from an interferometric standpoint, SAS platforms should be towed from a top-mounted attachment, as is the DARPA SAS, to suppress roll. Roll errors were identified as a primary source of error to interferometric systems in [9, 34] and a method for estimation and correction of these errors has been demonstrated on SAR data in [35].

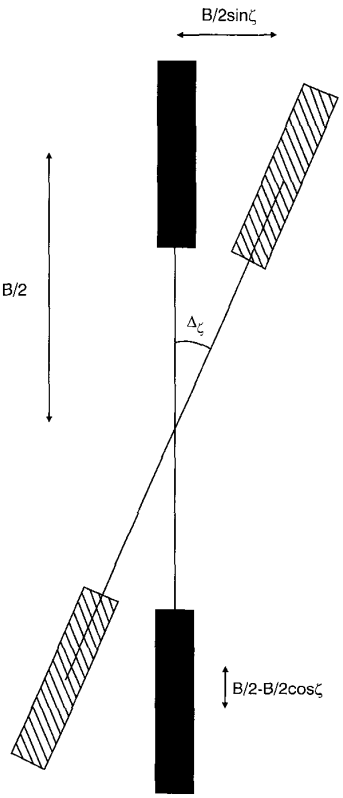

Fig. 10 *Effect of roll error on aperture location*

5.2 Imaging analysis

The above geometric analysis provides a good representation of the effects of motion, but is still not adequate. It does not take into account that motion errors will also affect the formation of the synthetic aperture images themselves, in the form of phase errors that consequently affect the interferometric calculation. Therefore, we also analysed the effect of motion based on an imaging model.

We can assume that, for small motion errors, the targets are affected by an along-track blurring function. Over small local areas, we can assume that this blurring function is identical for each point target so that our error model can be described by eqn. 8. Thus, the response at each pixel location can be represented by a superposition of target responses that blur across neighbouring pixels

$$\begin{aligned}\hat{g}_1(x_0, y_0) = a_1(x_0, y_0)\cdot h_1(y_0) \\ + a_1(x_0, y_0 \pm 1)\cdot h_1(y_0 \pm 1) + \ldots\end{aligned} \tag{26}$$

The phase difference at each pixel is calculated by measuring the angle of the response in image 1 multiplied by the complex conjugate of the response in image 2, so that the erroneous measurement can be described by

$$\angle\{\hat{g}_1(y_0)\cdot\hat{g}_2(y_0)\} = \angle\left\{\begin{array}{l} a_1(y_0)\cdot a_2(y_0)\cdot|h_1(y_0)|\cdot|h_2(y_0)| \\ \quad\cdot\exp(j(\angle h_1(y_0) - \angle h_2(y_0))) + \cdots \\ \cdots + a_1(y_0)\cdot a_2(y_0 \pm 1)\cdot|h_1(y_0)|\cdot|h_2(y_0 \pm 1)| \\ \quad\cdot\exp(j(\angle h_1(y_0) - \angle h_2(y_0 \pm 1))) + \cdots \\ \cdots + a_1(y_0 \pm 1)\cdot a_2(y_0 \pm 1)\cdot|h_1(y_0 \pm 1)|\cdot|h_2(y_0 \pm 1)| \\ \quad\cdot\exp(j(\angle h_1(y_0 \pm 1) - \angle h_2(y_0 \pm 1))) + \cdots \end{array}\right\} \tag{27}$$

where the x_0 term has been omitted for conciseness. In the case of two-pass imaging, the phase error function is different for each image, so that this phase difference measurement is corrupted by an error that is related to the reflectivity of adjacent scatterers multiplied by a combination of the phase error functions. We can model the combined error terms with a uniform distribution in phase. Thus, the height information is completely destroyed unless the separate phase error functions in each image can be estimated and removed.

In one-pass imaging, however, the phase error functions are assumed to be nearly identical for both images. That is, $h_1(y) \approx h_2(y)$. If the images are perfectly coregistered, as we are also assuming, then the magnitude distributions are also identical. Let us define the following functions to simplify the discussion:

$$X_1 = Ae^{j(\phi_A + \psi_{A1})} + Be^{j(\phi_B + \psi_{B1})} + Ce^{j(\phi_C + \psi_{C1})} + \cdots \tag{28}$$

$$X_2 = Ae^{j(\phi_A + \psi_{A2})} + Be^{j(\phi_B + \psi_{B2})} + Ce^{j(\phi_C + \psi_{C2})} + \cdots \tag{29}$$

X_1 and X_2 represent corresponding pixels in both images. A represents the magnitude contribution of data associated with the desired pixel location and B, C, ... represent

contributions that have blurred in from neighbouring pixels via the error function. The ideal pixel phase terms are represented by ψ and the phase error function terms, which are identical for both images, are represented by ϕ. The phase difference is found from

$$
\begin{aligned}
X_1 \cdot X_2^* = \\
& A^2 e^{j(\psi_{A1}-\psi_{A2})} + B^2 e^{j(\psi_{B1}-\psi_{B2})} + C^2 e^{j(\psi_{C1}-\psi_{C2})} + \cdots \\
& ABe^{j(\phi_A-\phi_B+\psi_{A1}-\psi_{B2})} + ABe^{j(\phi_B-\phi_A+\psi_{B1}-\psi_{A2})} + \cdots \\
& BCe^{j(\phi_B-\phi_C+\psi_{B1}-\psi_{C2})} + BCe^{j(\phi_C-\phi_B+\psi_{C1}-\psi_{B2})} + \cdots \\
& ACe^{j(\phi_A-\phi_C+\psi_{A1}-\psi_{C2})} + ABe^{j(\phi_C-\phi_A+\psi_{C1}-\psi_{A2})} + \cdots
\end{aligned}
\tag{30}
$$

where $\psi_{A1} - \psi_{A2}$ is the correct phase.

Since ϕ cancels out of the first terms of eqn. 30, it is apparent that the phase error function corrupts the phase difference measurement through the blurring of neighbouring pixels, adding zero-mean noise to the scene in an amount dependent upon the degree of image blurring. This can be removed via coherent pixel averaging [32]. Less obvious is the realisation that if the area height function is locally constant in along-track, eqn. 30 reduces to the correct phase difference. That is, $\psi_{A1} - \psi_{A2} = \psi_{B1} - \psi_{B2} = \psi_{C1} - \psi_{C2} = \psi_{A1} - \psi_{B2} = \psi_{B1} - \psi_{A2} = \psi_{A1} - \psi_{C2} = \cdots$. All of the ψ terms in eqn. 30 reduce to the correct phase measurement and, since it is an angular measurement, the phasor contributions associated with the ϕ terms cancel out. Therefore, the corruptive effect of motion errors in one-pass interferometric imaging is directly related to the along-track variability of the terrain height.

Fig. 11 verifies this conclusion. The returns from a field of over 100000 point targets, drawn from a 'rough' reflectivity distribution (Rayleigh in magnitude, uniform in phase), with discrete height shown in Fig. 11*b* were simulated as if collected by a platform affected by serious lateral errors. The processed SAS image is shown in Fig. 11*a*, with a strong point target included to highlight the image blur. Note that no height information is evident in the reflectivity image. Interferometric processing was performed on the corrupted images to form the height estimate Fig. 11*c*, without the aid of motion compensation or autofocus. The error distribution is shown in Fig. 11*d*. Examination reveals that it is directly related to the along-track variation of the height distribution of the field, as expected. Similar results were obtained by simulated data sets affected by other types of motion [11].

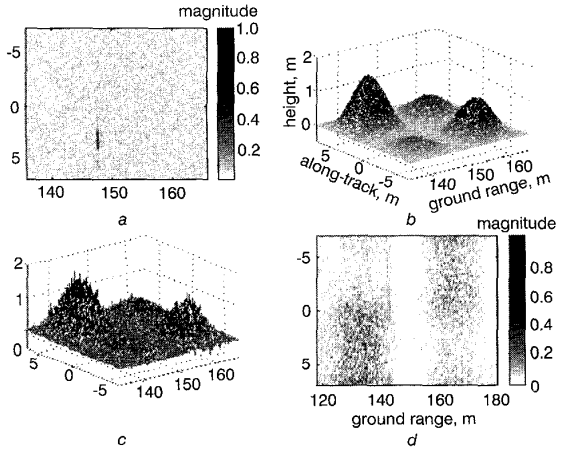

Fig. 11 *Simulated interferometric example*

We also studied the effect of each of the processing steps from Fig. 5 on the height estimate. We concluded that, if performed correctly, the motion compensation suite should restore the correct phase function to the data. That it, assuming that the correct motion errors are estimated, the correct phase will be restored. However, since these algorithms estimate relative motion between signal pings, they require some initial guess or *a priori* information to correctly integrate the motion error function across the aperture. It is not clear whether this information will always be available. Also, our motion compensation suite only corrects for yaw and sway, and not for phase errors inserted by other degrees of motion. The next step, image formation, is suitable for application to interferometry because both the ω–k and ACS algorithms are phase-preserving. Finally, the autofocus step, if performed in the manner described above, inserts a phase bias into each overlapping image strip during phase error estimation and correction, so is unsuitable for inclusion in an interferometric processing suite.

6 Conclusions

Based on our analysis, we conclude that in the absence of ideal conditions or extremely precise inertial measurement units, two-pass interferometric SAS is not feasible for a number of reasons. First and foremost, motion errors will have a more profound effect on two-pass interferometry through the separate phase error functions associated with each image. It is still unclear whether there is any way to remove and correct these errors in such a way to preserve the ideal phase function of the data. This is not possible utilising the autofocus described in this paper. Also, we did not discuss the effects of possible medium or target area variation between passes, which would affect the interferometric processing. Unfortunately, the precision of inertial instrumentation drives their cost [36], and the precision required for these operations apparently is not currently cost effective.

However, we also conclude that one-pass SAS interferometry, if performed so that roll errors are minimised, should be very robust against erroneous platform motion. SAS systems that are to be used for interferometric applications should therefore be designed to minimise roll motions. It is hypothesised that for slowly varying target height, SAS interferometry height measurements may be more robust with respect to other motion errors than the basic two-dimensional SAS image. In particular, our simulated results suggest that height information is recoverable even in some situations in which the conventional SAS reflectivity image is completely ruined by phase-error-induced blur.

7 Acknowledgments

The authors would like to thank DARPA, Raytheon, and Dynamics Technology, Inc. for supplying raw data sets in support of this research. They would specifically like to thank Dr. Enson Chang and Dr. Ralph Chatham for their helpful discussions and advice. The simulation code used in this study was based on code graciously supplied by Dr. Peter Gough and Dr. David Hawkins of the University of Canterbury, New Zealand, and is available at http://seal-www.gtri.gatech.edu/SPB.

8 References

1 MORRIS, G., and HARKNESS, L.: 'Airborne pulsed Doppler radar' (Artech House, Boston, 1996, 2nd edn.)

2 STOWE, D.W., WALLMAN, L.H., FOLLIN, J.W., and LUKE, P.J.: 'Stability of the acoustic pathlength of the ocean deduced from the medium stability experiment'. Technical Report TG 1230, Applied Physics Laboratory, John Hopkins University, 1974

3 CHRISTOFF, J.T., LOGGINS, C.D., and PIPKIN, E.L.: 'Measurement of the temporal phase stability of the medium', *J. Acoust. Soc. Am.*, 1982, **71**, (6), pp. 1606–1607

4 GOUGH, P.T., and HAYES, M.P.: 'Measurements of the acoustic phase stability in Loch Linne Scotland', *J. Acoust. Soc. Am.*, 1989, **86**, (2), pp. 837–839

5 CUTRONA, L.J.: 'Comparison of sonar system performance achievable using synthetic aperture techniques with the performance achievable by more conventional means', *J. Acoust. Soc. Am.*, 1975, **58**, (2), pp. 336–348

6 DE HEERING, P.: 'Alternate schemes in synthetic aperture sonar processing', *IEEE J. Ocean. Eng.*, 1984, **OE-9**, (4), pp. 277–280

7 GOUGH, P.T., and HAWKINS, D.W.: 'A short history of synthetic aperture sonar'. Proceedings of 1998 International Geoscience and Remote Sensing Symposium, IGARSS '98, 1998, **2**, pp. 618–620

8 GRAHAM, L.C.: 'Synthetic interferometer radar for topographic mapping', *Proc. IEEE*, 1974, **62**, (6), pp. 763–768

9 GRIFFITHS, H.D., RAFIK, T.A., MENG, Z., and COWAN, C.F.N.: 'Interferometric synthetic aperture sonar for high resolution 3-D mapping of the seabed', *IEE Proc., Radar Sonar Navig.*, 1997, **144**, (2), pp. 96–103

10 NELSON, M.A.: 'DARPA synthetic aperture sonar'. Proceedings of Adaptive Sensor Array Processing (ASAP) Workshop, 15 May 1998, **1**, pp. 141–155

11 BONIFANT, W.W.: 'Interferometric synthetic aperture sonar processing'. Masters Thesis, Georgia Institute of Technology, Atlanta, GA, 1999

12 WILLIAMS, R.E.: 'Creating an acoustic synthetic aperture in the ocean', *J. Acoust. Soc. Am.*, 1976, **60**, (1), pp. 60–73

13 LEE, H.E.: 'Extension of synthetic aperture radar (SAR) techniques to undersea applications', *IEEE J. Ocean. Eng.*, 1979, **4**, (2), pp. 60–63

14 LAWLOR, M.A., ADAMS, A.E., HINTON, O.R., RIYAIT, V.S., and SHARIFF, B.: 'Methods for increasing the azimuth resolution and mapping rate of a synthetic aperture sonar'. Proceedings of IEEE Oceans '94, 1994, **3**, pp. 565–570

15 TOMIYASU, K.: 'Tutorial review of synthetic-aperture-radar (SAR) with applications to imaging of the ocean surface', *Proc. IEEE*, 1978, **66**, (5), pp. 563–583

16 GOUGH, P.T., and HAWKINS, D.W.: 'Imaging algorithms for a strip-map synthetic aperture sonar: minimizing the effects of aperture errors and aperture undersampling', *IEEE J. Ocean. Eng.*, 1997, **22**, (1), pp. 27–38

17 SOUMEKH, M.: 'Fourier array imaging' (Prentice Hall, Englewood Cliffs, 1994)

18 KOCK, W.E.: 'Extending the maximum range of synthetic aperture (hologram) systems', *Proc. IEEE*, 1972, **60**, pp. 1459–1460

19 GILMOUR, G.A.: 'Synthetic aperture side-looking sonar system', *J. Acoust. Soc. Am.*, 1978, **65**, (2), pp. 557

20 SHERIFF, R.W.: 'Synthetic aperture beamforming with automatic phase compensation for high frequency sonars'. Proceedings of the IEEE 1992 Symposium on Autonomous Underwater Vehicle Technology, June 1992, pp. 236–245

21 RAVEN, R.S.: 'Electronic stabilization for displaced phase centers systems'. US Patent 4244036, 1981

22 TONARD, V., and BRUSSIEUX, M.: 'Towards development of autofocusing schemes for phase compensation of synthetic aperture sonars'. Proceedings of Oceans '97, Oct.1997, **2**, pp. 803–808

23 CAFFORIO, C., PRATTI, C., and ROCCA, F.: 'SAR data focusing using seismic migration techniques.', *IEEE Trans. Aerosp. Electron. Syst.*, 1991, **27**, pp. 199–207

24 HAWKINS, D.W., and GOUGH, P.T.: 'Synthetic aperture imaging using the accelerated chirp scaling algorithm'. 1997 International Geoscience and Remote Sensing Symposium, IGARSS '97, Aug. 1997, **1**, pp. 471–473

25 WAHL, D.E., EICHEL, P.H., GHIGLIA, D.C., and JAKOWATZ, C.V.: 'Phase gradient autofocus: a robust tool for high resolution SAR phase correction.', *IEEE Trans. Aerosp. Electron. Syst.*, 1994, **30**, (3), pp. 827–835

26 JAKOWATZ, C.V., WAHL, D.E., EICHEL, P.H., GHIGLIA, D.C., and THOMPSON, P.A.: 'Spotlight-mode synthetic aperture radar: A signal processing approach' (Kluwer Academic Publishers, Boston, 1996)

27 COOK, C.E., and BERNFELD, M.: 'Radar signals: An introduction to theory and application' (Academic Press, Boston, 1967)

28 WAHL, D.E., JAKOWATZ, C.V., and THOMPSON, P.A.: 'New approach to strip-map SAR autofocus.'. Proceedings of 6th IEEE DSP Workshop, Oct. 1994, pp. 53–56

29 HAWKINS, D.W.: 'Synthetic aperture imaging algorithms'. PhD Dissertation, University of Canterbury, Christchurch, New Zealand, 1996

30 JAKOWATZ, C.V., WAHL, D.E., EICHEL, P.H., GHIGLIA, D.C., and THOMPSON, P.A.: 'Spotlight mode synthetic aperture radar: a signal processing approach' (Kluwer, Boston, 1996)

31 GHIGLIA, D.C., and ROMERO, L.A.: 'Robust two-dimensional weighted and unweighted phase unwrapping that uses fast transforms and iterative methods', *J. Opt. Soc. Am.*, 1994, **11**, (1), pp. 107–117

32 LI, F., and GOLDSTEIN, R.M.: 'Studies of multibaseline spaceborne interferometric synthetic aperture radars', *IEEE Trans. Geosci. Remote Sens.*, 1990, **28**, pp. 88–97

33 RODRIGUEZ, E., and MARTIN, J.M.: 'Theory and design of interferometric synthetic aperture radars', *IEE Proc. - F*, 1992, **139**, (2), pp. 147–159

34 GRIFFITHS, H.: 'Interferometric synthetic aperture radar', *Electron Commun. Eng. J.*, 1995, **7**, (6), pp. 247–256

35 BULLOCK, R.J., VOLES, R., CURRIE, A., GRIFFITHS, H.D., and BRENNAN, P.V.: 'Two-look method for correction of roll errors in aircraft-borne interferometric SAR', *Electron Lett.*, 1997, **33**, (18), pp. 1581–1583

36 BRUCE, M.P.: 'A processing requirement and resolution capability comparison of side-scan and synthetic-aperture sonars', *IEEE J. Ocean. Eng.*, 1992, **17**, (1), pp. 106–117